

Optimum shape for metallic taper arrays to harvest light

Baocheng Zhu, Shiyi Xiao, and Lei Zhou*

*State Key Laboratory of Surface Physics and Key Laboratory of Micro and Nano Photonic Structures (Ministry of Education)
and Physics Department, Fudan University, Shanghai 200433, China*

(Received 29 April 2014; revised manuscript received 23 June 2014; published 9 July 2014)

Based on an effective-medium description for metallic taper arrays, we found that wave propagation inside these systems is governed by a Schrödinger-like equation with an effective potential solely determined by the taper shape. Such mapping not only helps us understand complicated wave-transporting phenomena in such systems but also yields an analytical criterion to identify the optimum taper shape. We applied the theory to design optimum taper arrays in different frequency domains, with their excellent light-harvesting abilities confirmed by full-wave simulations.

DOI: [10.1103/PhysRevB.90.045110](https://doi.org/10.1103/PhysRevB.90.045110)

PACS number(s): 81.05.Xj, 78.67.Pt, 42.25.Bs, 84.60.Bk

I. INTRODUCTION

Recently, a class of metallic taper structure has drawn much attention in photonic research [1–17]. These structures typically consist of array of metallic objects with gradually varying cross-section areas [see Fig. 1(a)] so that they can squeeze electromagnetic (EM) fields into subwavelength regions without much reflection within a broad frequency regime. As a result, such structures have been widely used in light-harvesting-related applications, including solar cell [1–3] and light absorber [4–8], and in imaging-related applications [9–17]. In those applications, one requires the taper structures to exhibit working bandwidths as wide as possible and to enhance local EM fields as high as possible yet keep the total device thicknesses as thin as possible. In other words, the taper structures should exhibit high transmissions for light over a wide frequency bandwidth in order to yield the best light-harvesting performances. An interesting scientific question is, within a fixed thickness, what is the optimum taper shape to realize the best functionalities?

Theoretically, both analytical [14,18–20] and numerical [1,2,21] methods have been employed to study the optical properties of such structures. Analytical understandings on these problems were typically achieved on linear-shaped tapers by solving the surface-mode motions on metallic tapers based on the adiabatic approximation [17–20,22]. However, strictly speaking, this approximation is valid only when the apex angle is small enough [17–20,22]. Moreover, such an analytical approach failed to yield an explicit criterion to help search for the optimum taper shape. While numerical simulations can yield highly accurate results for such structures, the calculations are time consuming; thus, complete optimization over all kinds of taper shapes is practically impossible. Most available calculations assumed a linear taper shape [8,22–24] for simplicity. Several taper shapes were already tried in experimental and numerical studies [2,16,17], but which one is the best and why one is better than another are not fully understood from the theoretical side. Therefore, a simple criterion derived from an analytical theory, which can help in understanding the inherent physics and finding the optimum taper shape, is highly desired.

Here, we derive a criterion to help search for the optimum shape of the metallic object in a taper array to yield the best light-harvesting effect. We first develop in Sec. II an effective-medium theory (EMT) for periodic arrays of tapers made by perfect electric conductors (PECs) and justify the EMT by comparing it with full-wave simulations. Based on the EMT, we show in Sec. III that waves inside these *inhomogeneous* taper structures are governed by a Schrödinger-like equation with an “*effective potential*” term solely dictated by the taper shape. Such a mapping not only simplifies our theoretical treatment but also yields a *simple and analytical* criterion to judge the performance of a given structure and thus helps us find an optimum taper shape. Finite-difference time-domain (FDTD) simulations [25] are performed on the optimum structure, showing that a significant field enhancement can be easily realized within an ultrawide frequency range. After extending the PEC-based theory to realistic metal cases in Sec. IV, we conclude our paper in Sec. V.

II. EFFECTIVE-MEDIUM THEORY FOR METALLIC TAPER ARRAYS

The system we consider is schematically shown in Fig. 1(a), which consists of metallic tapers arranged in a square lattice with periodicity P . As shown in Fig. 1(b), each taper has a fixed height of h , and the gap between two adjacent tapers at their bottoms is fixed as w . The taper shape can be arbitrary, described by a function $d(z)$, where d is the diameter of the taper at a given position z . Our aim is to find the optimum $d(z)$ function such that the taper structure can exhibit a wideband optical transparency.

In this paper we assume that $P \ll \lambda$ (λ is the working wavelength) so that the system can be described by an EMT. To illustrate the essential physics only, in Sec. II and III we will assume that the tapers are formed by PECs. Such an assumption is suitable for low-frequency domains (e.g., gigahertz to terahertz regimes) and can significantly simplify the theoretical treatment. The extension to realistic metal cases will be given in Sec. IV. In addition, here we only consider the normal-incidence situation, so only the parallel permittivity/permeability components of the system are relevant. To calculate the effective-medium parameters $\epsilon_{\text{eff}}(z)$, $\mu_{\text{eff}}(z)$ [26] of the taper system at a given position z , we consider a model system containing infinitely long metallic

*Corresponding author: phzhou@fudan.edu.cn

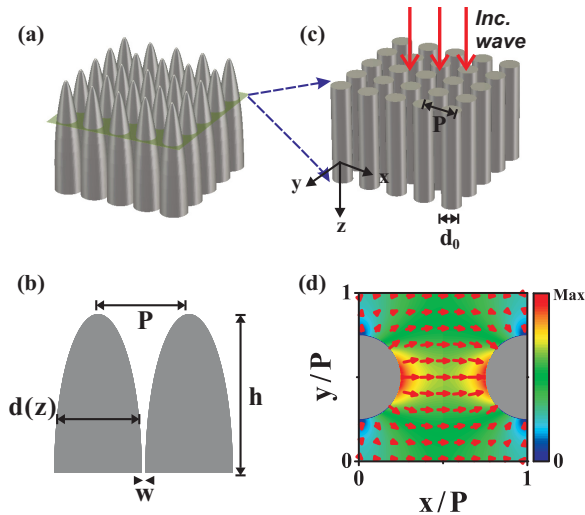


FIG. 1. (Color online) (a) Schematic picture of the periodic PEC tapers arranged in a square lattice. (b) Sectional view of the taper structure. (c) PEC cylinders with diameter d_0 arranged in the same square lattice as in (a). (d) \mathbf{E} -field distribution of the fundamental TEM mode in the PEC cylinder array with $d_0/P = 1/2$, with color representing the amplitude and arrows denoting the direction of the \mathbf{E} field.

cylinders with fixed diameter $d_0 = d(z)$ arranged in the same lattice [see Fig. 1(c)].

We followed a previously established homogenization scheme [27–30] to determine the effective-medium parameters of the model system depicted in Fig. 1(c). Shining a plane wave propagated in air normally onto the model medium, we can *rigorously* solve the wave-scattering problems by a standard mode-expansion technique. In the present case with $\lambda \gg P$, we can adopt the single-mode approximation to simplify our calculations, where only the fundamental modes in both regions are retained. Such an approximation is valid, since the higher-order diffraction modes in the air region are evanescent waves and the coupling strengths between the incident plane wave and all high-order modes inside the cylinder array are much smaller than that between two fundamental modes. Under the single-mode approximation, we found that the specular reflection coefficient takes the simple form [27] (see the Appendix for derivation details)

$$r_0 = \frac{|S_0|^2 - 1}{|S_0|^2 + 1}, \quad (1)$$

in which

$$S_0 = \frac{\int_{u.c} d\vec{r}_{||} (\vec{E}_{||}^{\text{inc}})^* \cdot \vec{E}_{0,||}^{\text{cyl}}}{\sqrt{\int_{u.c} d\vec{r}_{||} |\vec{E}_{||}^{\text{inc}}|^2 \cdot \int_{u.c} d\vec{r}_{||} |\vec{E}_{0,||}^{\text{cyl}}|^2}} \quad (2)$$

represents the overlapping between the incident wave and the fundamental mode inside the cylinder array. The integrals are performed within a unit cell. While it is difficult to *analytically* solve the eigenmodes in the cylinder array, one can always employ numerical simulations to obtain the field distribution $\vec{E}_0^{\text{cyl}}(x, y)$ associated with the fundamental mode, which is a transverse-electromagnetic (TEM) mode. Therefore, S_0 can be easily obtained numerically, which must be a function of

d_0/P . As an illustration, we depict in Fig. 1(d) the distribution of $\vec{E}_0^{\text{cyl}}(x, y)$ for a system with $d_0/P = 1/2$. Under the roughest approximation assuming a uniform \mathbf{E} -field distribution inside the hollow regions, we get approximately

$$|S_0|^2 \approx \frac{P^2 - \pi d_0^2/4}{P^2}. \quad (3)$$

The true dependence of S_0 on d_0/P is more complicated and could be determined by numerical simulations.

We now determine the effective parameters of the cylinder array. For a homogeneous medium with effective permittivity/permeability given by $\epsilon_{\text{eff}}, \mu_{\text{eff}}$, we understand that the normal-incidence reflection coefficient at the air–medium interface is simply

$$r_0 = \frac{Z_{\text{eff}} - 1}{Z_{\text{eff}} + 1}, \quad (4)$$

where $Z_{\text{eff}} = \sqrt{\mu_{\text{eff}}}/\sqrt{\epsilon_{\text{eff}}}$ is the impedance of the medium. Comparing Eq. (1) with Eq. (4), we find that the effective impedance Z_{eff} of the cylinder array is just $|S_0|^2$. On the other hand, under the single-mode approximation, we only need to consider the fundamental mode inside the cylinder array, which is a TEM mode exhibiting the same dispersion relation as a free mode in air. Therefore, we immediately understand that the effective refractive index $n_{\text{eff}} = \sqrt{\mu_{\text{eff}}} \cdot \sqrt{\epsilon_{\text{eff}}}$ of the cylinder array is just 1, corresponding to that of the fundamental TEM mode. These two equations help us uniquely determine the two effective parameters as

$$\mu_{\text{eff}} = \epsilon_{\text{eff}}^{-1} = |S_0|^2, \quad (5)$$

which can be easily calculated based on Eq. (2) after the field distribution of the fundamental TEM mode is known from FDTD simulations. Figure 2(a) shows how these two parameters, $\epsilon_{\text{eff}}, \mu_{\text{eff}}$, calculated by FDTD calculations, vary as functions of d_0/P . As d_0/P increases, we find that μ_{eff} decreases while ϵ_{eff} increases. This is because the hollow area in the system decreases so that $|S_0|^2$ is getting smaller. The analytical results calculated by Eq. (3) are shown as a green dotted line in Fig. 2(a), and they match reasonably with the numerical results especially in small d_0/P region. In the large d_0/P region, the \mathbf{E} -field distribution of the TEM mode deviates significantly from a uniform one, so the model results [obtained based on Eq. (3)] deviate obviously from full-wave simulations. Here, the effective parameters ($\epsilon_{\text{eff}}, \mu_{\text{eff}}$) do not exhibit frequency dispersions but only depend on the geometrical parameters. Similar conclusions hold for a one-dimensional stack of PEC slabs [28]. The inherent physics is that the fundamental modes in such PEC-based structures are TEM modes, so the effective refractive indexes do not exhibit any frequency dispersion.

To validate our EMT, we chose a typical system with $d_0/P = 1/2$ and $h/P = 5$ to calculate its reflection/transmission spectra by both FDTD simulations (on realistic structures) and EMT (on model systems), and we compared them in Fig. 2(b) [31]. The two calculations agree with each other quite well, which directly justified our EMT. The slight discrepancy appearing at the high-frequency region is because the single-mode approximation becomes insufficient in such region.

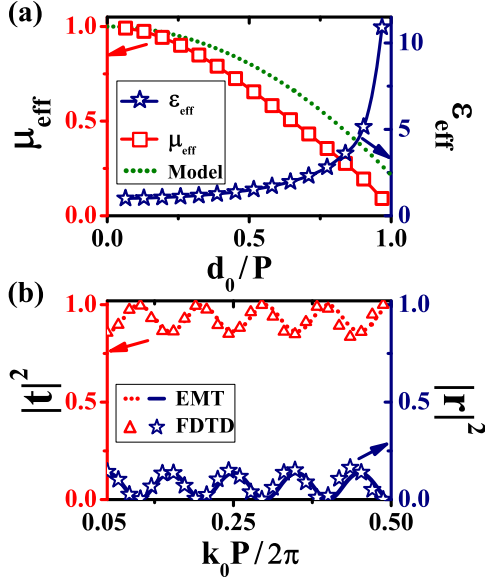


FIG. 2. (Color online) (a) ϵ_{eff} and μ_{eff} as functions of d_0/P calculated by numerical simulations (symbols), and μ_{eff} versus d_0/P obtained by analytical model Eq. (3) (dotted line). (b) Transmission and reflection spectra for a cylinder array with $d_0/P = 1/2$ and $h/P = 5$ calculated by both EMT on model systems (lines) and full-wave simulations on realistic structures (symbols).

Given an arbitrary taper structure, we can determine its effective parameter distributions ($\epsilon_{\text{eff}}(z), \mu_{\text{eff}}(z)$) by combining its shape function $d(z)$ with Fig. 2(a). To further justify our EMT on such *inhomogeneous* systems, we performed full-wave simulations on three taper structures and compare the obtained results with the corresponding EMT calculations. As shown in Fig. 3(a), the three taper structures exhibit the same height $h/P = 5$ and can be described by a unified shape function

$$d(z) = \alpha \cdot z^b, \quad (6)$$

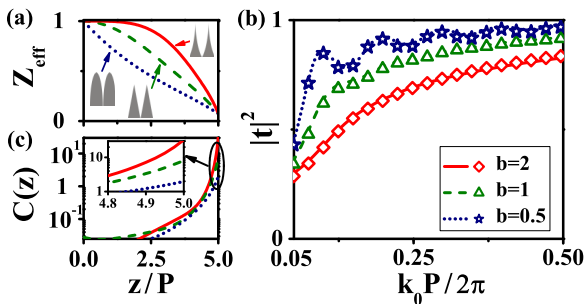


FIG. 3. (Color online) (a) Calculated effective impedance Z_{eff} versus z for three taper systems with the parameters $b = 2$ (red solid line), $b = 1$ (green dashed line), and $b = 0.5$ (blue dotted line). (b) Transmittance versus reduced frequency (here, $k_0 = \omega/c$) for three taper systems connected by semi-infinite cylinder arrays with $w/P = 0.02$, calculated by full-wave simulations on realistic systems (symbols) and EMT on the model system described by $\epsilon_{\text{eff}}(z), \mu_{\text{eff}}(z)$ (lines). (c) Distributions of the $C(z)$ function for three taper systems calculated at the frequency $k_0 P / 2\pi = 0.25$.

but they have different exponents b . Parameter α is fixed by the condition that all structures have the same gap width $w/P = 0.02$. Figure 3(a) shows how the effective impedance $Z_{\text{eff}}(z)$ of these systems varies as functions of z in different cases. For all these systems, their impedance Z_{eff} at $z = 0$ is always fixed at 1, since as $z \rightarrow 0$ the metallic objects gradually shrink their sizes to zero so that the systems just look like air. Meanwhile, $Z_{\text{eff}}(z = h)$ is fixed at a very small value dictated by w . The detailed z dependences of $Z_{\text{eff}}(z)$ are determined by the shape functions $d(z)$.

To minimize the reflections at the taper bottoms, we connected a semi-infinite cylinder array (with the same d/P value as that of the taper bottom) to all three taper structures and then performed FDTD simulations to calculate the transmission spectra of three systems for normally incident EM waves. With $\epsilon_{\text{eff}}(z), \mu_{\text{eff}}(z)$ known for all three systems (including the connecting homogeneous medium), we can easily solve the wave transmissions/reflections for the model system described by the EMT based on a standard transform matrix method. The EMT results on model systems are shown by lines in Fig. 3(b), which are in perfect agreement with the FDTD results [symbols in Fig. 3(b)] [31]. Such an excellent agreement justified our EMT developed for taper structures so that we can safely use the EMT to analyze and optimize the functionalities of these structures without suffering the heavy computation loads for FDTD simulations on realistic systems.

Several intriguing features are mentioned here. First, while all three taper structures attempt to guide light adiabatically from air to the connecting media, their light-harvesting functionalities are quite different and are highly dependent on the detailed taper shape. The convex taper ($b = 0.5$) performs better (in terms of the transmittance value and bandwidth) than the linear taper ($b = 1$), which in turn performs better than the concave one ($b = 2$). Second, the transmission spectrum in the $b = 0.5$ case exhibits characteristic oscillations, but such an intriguing effect is quite weak in other two cases. In the next section, we will develop an analytical theory to understand these intriguing observations and further derive a criterion to guide us to find the optimized taper shape yielding the best light-harvesting effect.

III. THE EFFECTIVE POTENTIAL APPROACH AND THE OPTIMUM TAPER SHAPE

Now that EMT calculations can yield highly reliable results for wave transmissions through such complicated structures, in this section, we employ the EMT to *analytically* study such problems. Such a simplification not only saves lots of computational effort but also helps get an *analytical* criterion for determining the best taper shape. EM-wave propagation inside such an inhomogeneous medium is governed by Maxwell's equations, which, under normal-incidence condition, are further reduced to the following equation for the **E** field:

$$\frac{\partial^2 E(z)}{\partial z^2} + 2\beta(z)\frac{\partial E(z)}{\partial z} + k_0^2 E(z) = 0, \quad (7)$$

where $k_0^2 = \omega^2/c^2$ and

$$\beta(z) = -\frac{1}{2} \frac{\partial [\ln Z_{\text{eff}}(z)]}{\partial z} = -\frac{1}{2} \frac{\partial [\ln \mu_{\text{eff}}(z)]}{\partial z}. \quad (8)$$

Here, we have already used the condition $\mu_{\text{eff}}(z) = \varepsilon_{\text{eff}}(z)^{-1}$. The equation satisfied by the \mathbf{H} field is similar to Eq. (7) but with a minus sign in front of $\beta(z)$.

Before solving Eq. (7), we first discuss the physical origin of β . The reflection coefficient of the EM wave at an interface between two homogeneous media with impedance Z_1 and Z_2 is $r = (Z_2 - Z_1)/(Z_2 + Z_1)$. Therefore, in an inhomogeneous medium with a position-dependent impedance function $Z(z)$, the reflection at position z can be written as $r = [Z(z + \Delta z) - Z(z)]/[Z(z + \Delta z) + Z(z)] = \Delta z \cdot \partial [\ln Z(z)] / 2\partial z$. Comparing the above expression with Eq. (8), we find that β just describes the reflection taking place in our medium centered at position z . In other words, β can be regarded as an effective internal reflection for the EM wave propagating inside an inhomogeneous medium.

We now turn to solving Eq. (7). Equation (7) contains a term proportional to $\partial E / \partial z$, making the problem difficult to handle. Such a term can be formally eliminated by the following transformation. By defining

$$E(z) = e^{-\int_0^z \beta(z') dz'} A(z), \quad (9)$$

and substituting Eq. (9) into Eq. (7), we find that the new function $A(z)$ satisfies

$$\frac{\partial^2 A(z)}{\partial z^2} - V(z)A(z) + k_0^2 A(z) = 0, \quad (10)$$

with

$$V(z) = \partial\beta(z)/\partial z + \beta^2(z). \quad (11)$$

After this transformation, the resulting Eq. (9) resembles Schrödinger's equation in quantum mechanics, with $V(z)$ playing the role of an *effective potential* term. The smaller the effective potential, the higher the transmittance. If we define a characteristic function as

$$C(z) = \frac{\partial\beta(z)/\partial z + \beta^2(z)}{k_0^2}, \quad (12)$$

then the criterion for realizing the best light-harvesting effect is

$$|C(z)| \ll 1. \quad (13)$$

For any taper with a definite shape function, one can always employ our theory to calculate its characteristic function $C(z)$ and then use Eq. (13) to check whether it is good or not. Including air and the connecting medium as part of the system when calculate the function $C(z)$, the reflections from the upper/bottom interfaces of the taper system are automatically considered. From Eqs. (12) and (13), not only the internal reflection term β but also its derivative $\partial\beta/\partial z$ contribute to the total reflections. Physically, the term $\partial\beta/\partial z$ comes from multiple reflections inside the inhomogeneous medium.

Apart from pure mathematical reasons of eliminating the $\partial E / \partial z$ term, the transformation Eq. (9) has a clear physical interpretation. Putting Eq. (8) into Eq. (9), we get $E(z) = \sqrt{\mu_{\text{eff}}(z)} A(z) = \sqrt{Z_{\text{eff}}(z)} A(z)$ where the relation $\mu_{\text{eff}} = (\varepsilon_{\text{eff}})^{-1}$ has been used. Since the energy flow in a medium with impedance Z is just $\langle \vec{S} \rangle = |E|^2 / 2Z$, we understand that it is $|A(z)|^2$, rather than $|E(z)|^2$, that represents the local energy flow. Therefore, solving an equation for $A(z)$

is more meaningful than solving the original equation for $E(z)$ [Eq. (7)].

We employed our theory to examine those examples studied in Sec. II in order to understand their distinct wave-transporting behaviors. Setting the frequency at $k_0 P / 2\pi = 0.25$, we calculated the $C(z)$ functions for those systems and compared the results in Fig. 3(c). While the criterion in Eq. (13) can be satisfied for three systems in most regions, it is drastically violated in the region $z \rightarrow h$, and such a violation is more severe for systems with larger b values [see inset to Fig. 3(c)]. This directly explains why the $b = 0.5$ taper exhibits the best wave-transmission properties within the three examples studied, since such a structure possesses the smallest $|C(z)|$ among all three systems considered.

The criterion in Eq. (13) can guide us to search for an optimized taper shape yielding the best light-harvesting effect. First, the β function is not entirely arbitrary but rather is subject to the following constraint:

$$\int_0^h \beta dz = -\frac{1}{2} \int_0^h \frac{\partial \ln Z_{\text{eff}}}{\partial z} dz = -\frac{1}{2} \ln Z_{\text{eff}}(h), \quad (14)$$

where $Z_{\text{eff}}(h)$ is a constant value fixed by the bottom gap width w . To minimize $C(z)$ *everywhere* inside the taper medium, a naïve guess solution is to set β *independent* of z , i.e.,

$$\beta(z) \equiv -\frac{\ln Z_{\text{eff}}(h)}{2h}, \quad (15)$$

and thus $\partial\beta(z)/\partial z = 0$. Because there is a β^2 term in $C(z)$ [see Eq. (12)], any attempt to lower $\beta^2(z)$ at a particular position must increase $\beta^2(z)$ at another position due to the constraint in Eq. (14), leading to overall enhanced $C(z)$ and thus enhanced reflections. Therefore, Eq. (15) is a natural choice to minimize $C(z)$. Still choosing the frequency at $k_0 P / 2\pi = 0.25$, we show the $C(z)$ distribution for the structure satisfying Eq. (15) as a black line in Fig. 4(a), which is a constant inside the taper

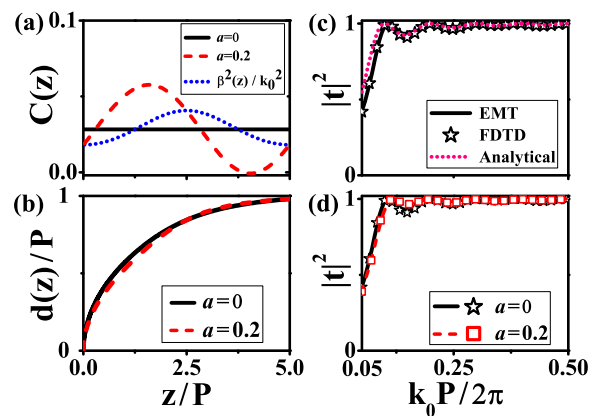


FIG. 4. (Color online) (a) $C(z)$ distributions for two taper systems described by Eq. (17) but with different values of a . The blue dotted line represents the distribution of the $\beta^2(z)/k_0^2$ function in the case of $a = 0.2$. (b) The corresponding shape functions $d(z)$ for the cases with $a = 0$ and 0.2 . (c) Transmission spectra of the taper system with $a = 0$, calculated by FDTD simulations (stars), EMT (solid line), and the analytical model in Eq. (16) (dotted line). (d) Transmission spectra of two taper systems with $a = 0$ and 0.2 , calculated by FDTD simulations (symbols) and EMT (lines).

region and is much smaller than 1. With the $\beta(z)$ function known [Eq. (15)], we can easily retrieve the corresponding shape function $d(z)$ of the taper through Eq. (8) and Fig. 2(a). The obtained shape function is depicted in Fig. 4(b) as a solid black line. Using such a structure, we employed both FDTD simulations (on a realistic system) and EMT calculations (on a model system) to study its transmission spectra and compared the results in Fig. 4(c). As expected, the EMT results are in perfect agreement with the FDTD ones, and both show that the transmittance can be nearly 100% in an ultrawide-frequency regime.

However, characteristic oscillations exist in both spectra for such a system even through its overall functionality is quite satisfactory. Such an oscillation also exists in some of our nonoptimized structures [see Fig. 3(c)]. We found that such an intriguing effect is contributed by the reflections at two interfaces. Since both the air region (where the incident light comes from) and the connecting medium (where the transmitted light goes) are homogeneous, and thus we have $\beta(z) \equiv 0$ in these regions, the $\beta(z)$ function is *discontinuous* at the air–taper and taper–connecting medium interfaces. Such discontinuity results in two δ -function potentials in the effective potential $V(z)$ [see Eq. (11)], leading to nonnegligible reflections. The Fabry-Perot (FP) interferences of waves reflected by two interfaces form the characteristic oscillations in the transmission spectrum. Since Fig. 4(a) shows that $C(z)$ is very small inside the system satisfying Eq. (15), we can safely neglect the effective potential term *inside* the taper region but only retain the two δ -function potentials at two interfaces. With such an approximation, we find that the transmittance satisfies [32]:

$$T = \left| \frac{4k_0^2}{4k_0^2 + 2ik_0(\beta(0) - \beta(h)) + \beta(0)\beta(h)(1 - e^{2ik_0h})} \right|^2. \quad (16)$$

Calculation results obtained with Eq. (16) are depicted as a dotted line in Fig. 4(c), which perfectly reproduced the characteristic oscillations in both FDTD and EMT spectra. In addition, such an analytical model naturally explains that the lower band edge of the transmission band is not an intrinsic quantity but is determined by the total height h of the taper structure. However, when reflections inside the taper medium are strong, such FP interferences cannot be well established. This explains why such characteristic oscillations do *not* exist in certain systems [see the $b = 1$ and $b = 2$ cases in Fig. 3(b)] because they are “dirty” systems with internal reflection that is too strong to dampen the FP oscillations.

The above analyses show that Eq. (15) is still *not* the final solution for the optimized taper shape due to the undesired FP oscillations in the spectrum. From Eq. (16), the strength of such an oscillation is determined by the coefficient $\beta(0)\beta(h)$, namely, the product of the two interface potentials. Therefore, we can slightly adjust the β function based on Eq. (15) so that the value $\beta(0)\beta(h)$ is lowered a bit but the effective potential inside the inner taper region is still small enough. There are a variety of $\beta(z)$ functions to satisfy such a requirement. Here, as an example, we assume that the $\beta(z)$ function takes the

following form:

$$\beta(z) = -\frac{\ln Z_{\text{eff}}(h)}{2h} \left[1 - a \cdot \cos\left(2\pi \frac{z}{h}\right) \right], \quad (17)$$

where the coefficient a is an adjustable parameter. By careful optimizations, we found that $a = 0.2$ is the best choice within all the cases satisfying Eq. (17).

As an illustration, we depicted the calculated $\beta^2(z)/k_0^2$ profile in Fig. 4(a) as a dotted line for the case of $a = 0.2$. Compared to the initial-guess solution ($a = 0$), here β^2 gets smaller at two interfaces. The shape function $d(z)$ for this new solution is depicted in Fig. 4(b) as a dashed line. With such an optimized shape, we recalculated the transmission spectra by both FDTD simulations (on a realistic structure) and EMT (on a model system), and found that the obtained results [squares and the dashed line in Fig. 4(d)] exhibit much suppressed oscillations, consistent with theoretical analyses. In such a structure, $\beta^2(0)$ and $\beta^2(h)$ are still nonzero. While we can enlarge a to further suppress the oscillations by lowering the value of $\beta(0)\beta(h)$, the overall reflections will enhance simultaneously because $C(z)$ will be enlarged significantly in the middle part of the taper medium. The optimized structure is obtained by carefully compromising these two effects. Different from the present scheme to directly suppress the reflections at two individual interfaces, antireflections can also be achieved based on the scattering cancellation mechanism using metamaterial multilayer coating [33–35]. However, such scattering cancellations can only be realized at certain frequencies so that the working frequency bandwidth is typically narrow [33–35].

We emphasize that the optimum taper structure also works well for oblique-incidence cases, although it is designed only based on normal-incidence considerations. FDTD simulations show that the transmittance of the optimized taper structure can remain over 80% up to a large angle of incidence $\theta = 60^\circ$ for both transverse-electric and transverse-magnetic polarizations over an ultrawide-frequency bandwidth (see the Supplemental Material [36]).

Having such an amazing wideband transparency for light, these taper structures can possess many applications in practice, especially in light-harvesting-related applications. As an illustration, we show in Fig. 5(a) the calculated \mathbf{E} -field pattern

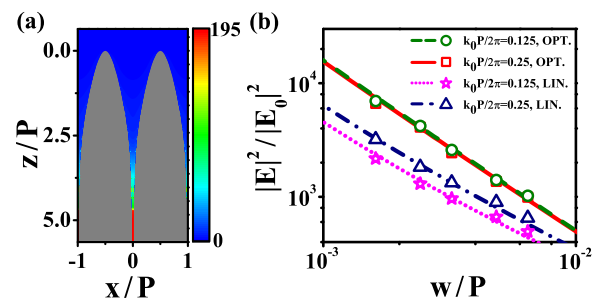


FIG. 5. (Color online) (a) Distribution of $|E|^2/|E_0|^2$ inside the optimized taper array (with $w/P = 0.02$ and $h/P = 5$) shined by a normally incident light with $k_0 P/2\pi = 0.25$. (b) Field enhancement as functions of the gap width w for two taper systems (with an optimized or a linear shape), calculated by FDTD simulations (symbols) and EMT (lines) at two frequencies $k_0 P/2\pi = 0.125, 0.25$.

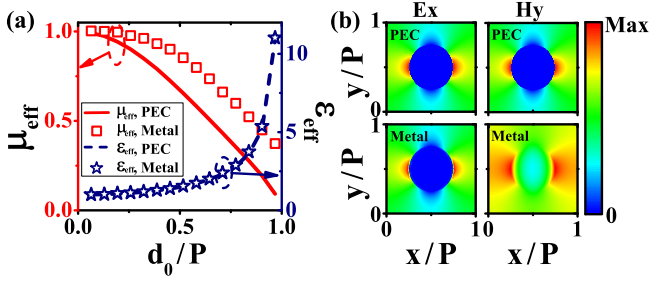


FIG. 6. (Color online) (a) ϵ_{eff} and μ_{eff} as functions of d_0/P for cylinder arrays made by realistic metals (symbols) or PECs (lines). (b) E_x and H_y amplitude distributions of the fundamental mode in cylinder arrays (with $d_0/P = 0.5$) made by realistic metals or PECs.

inside the optimized taper array (with parameters $a = 0.2$, $h/P = 5$, and $w/P = 0.02$), as it is illuminated by a normally incident light at frequency $k_0 P/2\pi = 0.25$. We found that the incident light is squeezed into the taper structure without suffering much reflection, so the local intensity of the \mathbf{E} field is significantly enhanced inside the tiny gaps in the connecting medium. In addition, a smaller bottom gap width can better squeeze the light, yielding a stronger local field enhancement. Figure 5(b) shows how the local field enhancement depends on the bottom gap width w for input light with frequencies $k_0 P/2\pi = 0.125$ and 0.25 . Similar functionalities at distinct frequencies demonstrated the wideband transparency property of the device. Compared to the nonoptimized linear taper shape, the optimized tapers exhibit much enhanced local field strengths within a broad frequency band. Again, we note the excellent agreement between the FDTD simulations and our EMT model calculations. This is particularly important for future applications, since FDTD simulations are extremely time consuming for tiny-gap taper arrays, which can be handled by our method easily.

IV. EXTENSIONS TO REALISTIC METAL CASES

The theory developed above can only be applied to PEC tapers, but at high frequencies metals cannot be described by PECs. In this section, we briefly describe how to extend our theory to realistic metal cases.

Following the strategy described in the previous two sections, we first need to know the effective ϵ_{eff} and μ_{eff} for a cylinder array [Fig. 1(c)] made by realistic metals. There are several EMTs available to do the job, and here we chose to extend the EMT developed for PEC cylinders (Sec. II) to realistic metal cases [37]. Setting the working wavelength as $1.55 \mu\text{m}$ and the periodicity of the cylinder array as $P = 0.2 \mu\text{m}$, we employed the extended EMT to calculate the ϵ_{eff} and μ_{eff} of systems with different cylinder diameters d and plotted the results in Fig. 6(a). Here, the metal is assumed as Au described by a Drude model with plasma frequency $\omega_p = 1.37 \times 10^{16}$ Hz [38]. We purposely set the collision frequency γ as zero when determine the ϵ_{eff} and μ_{eff} , since we want to clearly separate the effects contributed by absorption and the taper shape. It is trivial to take absorption back into our consideration.

Compared with the results obtained by the PEC-based EMT, we found that here ϵ_{eff} remains almost unchanged while μ_{eff}

changes a lot. To understand this point, we show the calculated E_x and H_y field distributions inside the cylinder array with $d_0/P = 0.5$ for both realistic metal and PEC cases [Fig. 6(b)]. It is clear that EM fields can penetrate inside realistic metals so that the local fields on the metallic surfaces are no longer as significant as those in PEC cases. Such an effect can obviously decrease the diamagnetic effect of the screening current, which leads to a less reduced μ_{eff} as compared to the PEC case. However, the influence of such an effect on ϵ_{eff} is relatively less significant, since ϵ_{eff} has a rather large background value.

We now extend the theory developed in Sec. III to a realistic metal case. Unlike in the PEC case, here the effective-medium properties of the taper array are dependent on frequency due to the dispersion of realistic metals. However, we found that such dispersion is weak, and our later results show that the taper structure designed at a target wavelength of $\sim 1.55 \mu\text{m}$ works well over a wide wavelength range. Meanwhile, since here $\epsilon_{\text{eff}}(z) \cdot \mu_{\text{eff}}(z) \neq 1$ [see Fig. 6(a)], the Schrödinger-like equation in Eq. (10) cannot be applied naively. The physical reason is that the fundamental mode inside such a cylinder array is no longer a TEM mode as in the PEC case. However, this problem can be remedied by changing the original coordinate z to a new one u , which describes the “optical length” experienced by light propagating inside the medium. Let us define [39]

$$u(z) = \frac{1}{L} \int_0^z n_{\text{eff}}(z') dz', \quad (18)$$

where $n_{\text{eff}}(z) = \sqrt{\epsilon_{\text{eff}}(z) \cdot \mu_{\text{eff}}(z)}$ is the local refractive index at position z and $L = \int_0^h n_{\text{eff}}(z') dz'$ is the total optical length inside the taper. Here, L are different for tapers with different shapes, so we define the variable $u(z)$ as the “normalized” optical length [see Eq. (18)] in order to compare different shapes on the same footing. Define the function $A(u)$ similar to Eq. (9) but in terms of the new coordinate u , we proved that the function $A(u)$ still satisfies a Schrödinger-like equation (see the Appendix for derivation details),

$$\frac{\partial^2 A(u)}{\partial u^2} - V(u)A(u) + k_0^2 L^2 A(u) = 0, \quad (19)$$

where the effective potential is defined as $V(u) = \partial\beta(u)/\partial u + \beta^2(u)$, in which

$$\beta(u) = -\frac{\partial [\ln Z_{\text{eff}}(u)]}{2\partial u}, \quad (20)$$

with $Z_{\text{eff}}(u) = \sqrt{\mu_{\text{eff}}(u)}/\sqrt{\epsilon_{\text{eff}}(u)}$ as the effective impedance. Remarkably, we find that except the multiplier L^2 in the third term of Eq. (19), all these equations exhibit the same forms as those presented in Sec. III if we replace the coordinate z with u . Equation (19) can be regarded as a generalized Schrödinger-like equation for EM waves inside general metallic taper systems and can recover the specific form of Eq. (10) in the limit of a PEC. Therefore, based on the discussions presented in Sec. III, we find that the optimum taper shape for a realistic metal case should be determined by

$$\beta(u) = -\frac{\ln(Z_{\text{eff}}|_{u=1})}{2} [1 - 0.2 \cdot \cos(2\pi u)]. \quad (21)$$

Combining Eq. (21) with Eq. (20), we can determine the $Z_{\text{eff}}(u)$ function for the optimum taper shape. Further

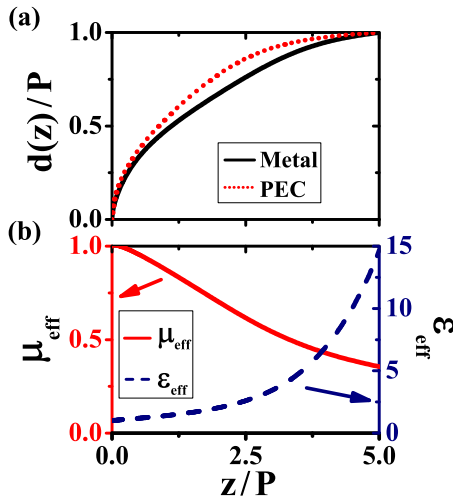


FIG. 7. (Color online) (a) Optimized taper shape functions, obtained by the theories developed for realistic metal (solid line) and PEC (dotted line). (b) $\epsilon_{\text{eff}}(z)$ and $\mu_{\text{eff}}(z)$ of the designed optimum taper array.

combining the obtained $Z_{\text{eff}}(u)$ with Eq. (18), as well as Fig. 6(a), we can numerically retrieve the shape function $d(z)$ for the optimum taper shape. Setting $w/P = 0.02$, $h/P = 5$, and $P = 0.2\mu\text{m}$, we successfully retrieved the optimum shape function and plotted the result as a solid line in Fig. 7(a). The optimum shape for a realistic metal taper deviates slightly from the PEC solution (dotted line), indicating that the finite field penetration in a realistic metal has nonnegligible effects.

To verify the theoretical predictions, we employed FDTD simulations to calculate the transmission spectrum of a metallic taper array with an optimized shape function. Similar to Sec. III, again we assumed that the taper structure is connected with an infinite cylinder array as a guiding medium. As a comparison, we also calculated the effective-medium properties (i.e., $\epsilon_{\text{eff}}(z), \mu_{\text{eff}}(z)$) of the designed taper array [Fig. 7(b)] and employed a standard transfer-matrix method to study the transmission spectrum of the model system based on the EMT. Figure 8 compares the transmission spectra of the designed taper array calculated by both FDTD simulations (dotted line)

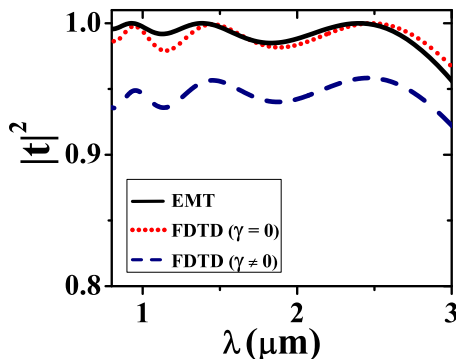


FIG. 8. (Color online) Transmission spectra through the designed optimum taper structure, calculated by the EMT based on the model system described by $\epsilon_{\text{eff}}(z)$ and $\mu_{\text{eff}}(z)$ and FDTD simulations based on realistic systems with loss neglected (dotted line) and included (dashed line).

and EMT (solid line), which are in good agreement with each other. Both results show that such a taper structure, designed at a target wavelength $\lambda = 1.55\mu\text{m}$, can support nearly total transmission for light over a wide frequency regime of $\sim 1.55\mu\text{m}$. Even taking losses of realistic metals into consideration, we found that the transmittance persists to a high value over the frequency domain of interests, as shown by the corresponding FDTD simulation results (dashed line in Fig. 8) and assuming that $\gamma = 4.08 \times 10^{13}\text{Hz}$ [38] in the Drude model for Au.

V. CONCLUSIONS

We have established a theory to guide searching for the optimum shape functions for metallic taper arrays to harvest light. We applied the theory to low- and high-frequency regimes and found by full-wave simulations that the designed optimum structures exhibit excellent wideband light-harvesting functionalities. Many applications of our theory can be expected, and we are looking forward to experimental verifications.

ACKNOWLEDGMENTS

This paper was supported by the National Natural Science Foundation of China (Grant No. 11174055), the Program of the Shanghai Subject Chief Scientist (Program No. 12XD1400700), and Ministry of Education of China (Grant No. B06011).

APPENDIX

1. Derivation of Eq. (1)

As shown in Fig. 1(c), consider a semi-infinite PEC cylinder array illuminated by a normally incident x -polarized plane wave. The incident fields can be written as

$$\begin{aligned}\vec{H}^{\text{inc}} &= \frac{1}{Z_0 P} e^{ik_0 z} \hat{e}_y \\ \vec{E}^{\text{inc}} &= \frac{1}{P} e^{ik_0 z} \hat{e}_x,\end{aligned}\quad (\text{A1})$$

where Z_0 is the impedance of air, $k_0 = \omega/c$, and P is the lattice constant.

Bloch theory tells us that the reflected wave can be written as

$$\begin{aligned}\vec{H}^{\text{ref}} &= r_0 \vec{H}_0 + \sum_{m \neq 0, n \neq 0, \sigma = s, p} r_{m,n}^{\sigma} \vec{H}_{m,n}^{\sigma} \\ \vec{E}^{\text{ref}} &= r_0 \vec{E}_0 + \sum_{m \neq 0, n \neq 0, \sigma = s, p} r_{m,n}^{\sigma} \vec{E}_{m,n}^{\sigma},\end{aligned}\quad (\text{A2})$$

where the eigenmode wave functions are explicitly given by

$$\begin{aligned}\vec{E}_0 &= \frac{1}{P} e^{-ik_0 z} \hat{e}_x \\ \vec{E}_{m,n}^s &= (-\hat{e}_x \sin \theta_{m,n} + \hat{e}_y \cos \theta_{m,n}) \frac{1}{P} e^{i(k_x^m x + k_y^n y)} e^{-ik_z^{m,n} z} \\ \vec{E}_{m,n}^p &= (\hat{e}_x \cos \theta_{m,n} + \hat{e}_y \sin \theta_{m,n}) \frac{1}{P} e^{i(k_x^m x + k_y^n y)} e^{-ik_z^{m,n} z},\end{aligned}\quad (\text{A3})$$

in which $k_x^m = 2m\pi/P$, $k_y^n = 2n\pi/P$, $\theta_{m,n} = \tan^{-1}(n/m)$, $k_z^{m,n} = \sqrt{k_0^2 - (k_x^m)^2 - (k_y^n)^2}$. In addition, r_0 is the specular reflection coefficient, and $r_{m,n}^\sigma$ denote the reflection coefficients for diffraction channels with different mode index and polarization. The corresponding \mathbf{H} fields can be derived from Eq. (A3) by Maxwell's equations easily. These eigenmodes satisfy the following orthonormal conditions:

$$\begin{aligned} \langle \vec{E}_0 | \vec{E}_{m,n}^\sigma \rangle &= \int_{u.c.} \vec{E}_0^* \cdot \vec{E}_{m,n}^\sigma dx dy = 0 \\ \langle \vec{E}_{m,n}^\sigma | \vec{E}_{m',n'}^{\sigma'} \rangle &= \int_{u.c.} \vec{E}_{m,n}^{\sigma*} \cdot \vec{E}_{m',n'}^{\sigma'} dx dy = \delta_{\sigma\sigma'} \delta_{mm'} \delta_{nn'} \quad \sigma = s, p, \end{aligned} \quad (\text{A4})$$

where the integrals are performed within a unit cell.

The transmitted wave inside the PEC cylinder array can also be formally expressed as

$$\begin{aligned} \vec{H}^t &= \sum_q t_q \vec{H}_q^{\text{cyl}} \\ \vec{E}^t &= \sum_q t_q \vec{E}_q^{\text{cyl}}, \end{aligned} \quad (\text{A5})$$

where t_q are the transmission coefficients and the index q runs over all possible eigenmodes inside such a medium subject to the Bloch condition

$$\begin{aligned} \vec{H}_q^{\text{cyl}}(\vec{r} + nP\hat{x} + mP\hat{y}) &= \vec{H}_q^{\text{cyl}}(\vec{r}) \\ \vec{E}_q^{\text{cyl}}(\vec{r} + nP\hat{x} + mP\hat{y}) &= \vec{E}_q^{\text{cyl}}(\vec{r}). \end{aligned} \quad (\text{A6})$$

Due to the translational invariance along the z direction, these eigen wavefunctions can be generally written as $\vec{E}_q^{\text{cyl}}(\vec{r}) = \vec{E}_q^{\text{cyl}}(x, y) e^{\pm ik_q z}$, $\vec{H}_q^{\text{cyl}}(\vec{r}) = \vec{H}_q^{\text{cyl}}(x, y) e^{\pm ik_q z}$. These eigenmodes can be obtained by numerical simulations or other computational approaches such as the multiple-scattering method, and they must satisfy the following orthonormal conditions:

$$\begin{aligned} \langle \vec{E}_q^{\text{cyl}}(x, y) | \vec{E}_{q'}^{\text{cyl}}(x, y) \rangle &= \int_{u.c.} (\vec{E}_q^{\text{cyl}}(x, y))^* \cdot \vec{E}_{q'}^{\text{cyl}}(x, y) dx dy = \delta_{qq'} \\ \langle \vec{H}_q^{\text{cyl}}(x, y) | \vec{H}_{q'}^{\text{cyl}}(x, y) \rangle &= \int_{u.c.} (\vec{H}_q^{\text{cyl}}(x, y))^* \cdot \vec{H}_{q'}^{\text{cyl}}(x, y) dx dy = \delta_{qq'}, \end{aligned} \quad (\text{A7})$$

where the integrals are performed within the air region inside a unit cell.

By matching the boundary conditions at $z = 0$ for the \mathbf{H} and \mathbf{E} fields and fully utilizing the orthonormal conditions in Eqs. (A4) and (A7), we get the following set of linear equations to determine the coefficients:

$$\begin{aligned} X_q^{\text{cyl}} \left[\frac{1 - r_0}{Z_0} (S_{0;q})^* - \sum_{m \neq 0, n \neq 0} \left(\frac{r_{m,n}^p}{Z_{m,n}} (S_{m,n;q}^p)^* + Y_{m,n} r_{m,n}^s (S_{m,n;q}^s)^* \right) \right] &= t_q \\ 1 + r_0 &= \sum_q t_q S_{0;q} \\ r_{m,n}^\sigma &= \sum_q t_q S_{m,n;q}^\sigma, \end{aligned} \quad (\text{A8})$$

where $Z_{m,n} = k_z^{m,n}/\omega\epsilon_0$ and $Y_{m,n} = k_z^{m,n}/\omega\mu_0$, the overlapping integrals are defined as

$$\begin{aligned} S_{0;q} &= \frac{\int_{u.c.} d\vec{r}_{||} (\vec{E}_{||}^{\text{inc}})^* \cdot \vec{E}_{q,||}^{\text{cyl}}}{\sqrt{\int_{u.c.} d\vec{r}_{||} |\vec{E}_{||}^{\text{inc}}|^2 \cdot \int_{u.c.} d\vec{r}_{||} |\vec{E}_{q,||}^{\text{cyl}}|^2}} \\ S_{m,n;q}^\sigma &= \frac{\int_{u.c.} d\vec{r}_{||} (\vec{E}_{m,n,||}^\sigma)^* \cdot \vec{E}_{q,||}^{\text{cyl}}}{\sqrt{\int_{u.c.} d\vec{r}_{||} |\vec{E}_{m,n,||}^\sigma|^2 \cdot \int_{u.c.} d\vec{r}_{||} |\vec{E}_{q,||}^{\text{cyl}}|^2}}, \end{aligned} \quad (\text{A9})$$

and

$$X_q^{\text{cyl}} = \begin{cases} k_q/\omega\epsilon_0, & q \text{ is a TM mode} \\ \omega\mu_0/k_q, & q \text{ is a TE mode.} \end{cases} \quad (\text{A10})$$

The overlapping integral between two fundamental modes in different regions is certainly much stronger than others,

i.e., $S_{m,n;q}^\sigma \ll S_{0;q} \ll S_{0;0} = S_0$. Therefore, we take the single-mode approximation to retain only the fundamental modes in both air and cylinder array regions, which is equivalent to setting $S_{m,n;q}^\sigma = 0$ and $S_{0;q} = 0$ (for $q \neq 0$) in Eq. (A8). Furthermore, the fundamental mode in the cylinder array is a TEM mode with $X_0^{\text{cyl}} = Z_0$, and we get from

Eq. (A8) that

$$\begin{aligned} (1 - r_0) \cdot S_0^* &= t_0 \\ (1 + r_0) &= t_0 S_0. \end{aligned} \quad (\text{A11})$$

Equation (A11) tells us that the specular reflection coefficient is

$$r_0 = \frac{|S_0|^2 - 1}{|S_0|^2 + 1}, \quad (\text{A12})$$

which is just Eq. (1) in the main text.

2. Derivation of Eq. (19)

Considering Maxwell's equations inside a one-dimensional inhomogeneous medium described by $\varepsilon_{\text{eff}}(z), \mu_{\text{eff}}(z)$, we can easily derive the equation for the \mathbf{E} field as

$$\frac{\partial^2 E(z)}{\partial z^2} - \frac{\partial \mu_{\text{eff}}(z)}{\mu_{\text{eff}}(z) \partial z} \frac{\partial E(z)}{\partial z} + k_0^2 n_{\text{eff}}^2(z) E(z) = 0, \quad (\text{A13})$$

where $n_{\text{eff}}(z) = \sqrt{\varepsilon_{\text{eff}}(z) \cdot \mu_{\text{eff}}(z)}$ is the refractive index at position z . Define a new coordinate u as $u(z) = \int_0^z n_{\text{eff}}(z') dz' / L$,

with $L = \int_0^h n_{\text{eff}}(z') dz'$, we can rewrite Eq. (A13) as

$$\frac{\partial^2 E(u)}{\partial u^2} + 2\beta(u) \frac{\partial E(u)}{\partial u} + k_0^2 L^2 E(u) = 0, \quad (\text{A14})$$

where $\beta(z) = -\partial [\ln Z_{\text{eff}}(u)] / 2\partial u$ and $Z_{\text{eff}}(u) = \sqrt{\mu_{\text{eff}}(u)} / \sqrt{\varepsilon_{\text{eff}}(u)}$.
Defining

$$E(u) = e^{-\int_0^u \beta(u') du'} A(u) \quad (\text{A15})$$

and substituting Eq. (A15) into Eq. (A14), we find $A(u)$ satisfies

$$\frac{\partial^2 A(u)}{\partial u^2} - V(u) A(u) + k_0^2 L^2 A(u) = 0, \quad (\text{A16})$$

where $V(u) = \partial \beta(u) / \partial u + \beta^2(u)$. Equation (A16) is the desired result, as shown in Eq. (19) in the main text.

-
- [1] K. X. Wang, Z. Yu, V. Liu, Y. Cui, and S. Fan, *Nano Lett.* **12**, 1616 (2012).
- [2] W. Zhou, M. Tao, L. Chen, and H. Yang, *J. Appl. Phys.* **102**, 103105 (2007).
- [3] L. Chen, W. E. I. Sha, and W. C. H. Choy, *Opt. Express* **20**, 8175 (2012).
- [4] Y. Cui, K. H. Fung, J. Xu, H. Ma, Y. Jin, S. He, and N. X. Fang, *Nano Lett.* **12**, 1443 (2012).
- [5] J. Zhu, Z. Yu, G. Burkhard, C. Hsu, S. Connor, Y. Xu, Q. Wang, M. McGehee, S. Fan, and Y. Cui, *Nano Lett.* **9**, 279 (2009).
- [6] S. Zhang, Y. Li, G. Feng, B. Zhu, S. Xiao, L. Zhou, and L. Zhao, *Opt. Express* **19**, 20462 (2011).
- [7] E. Rephaeli and S. Fan, *Appl. Phys. Lett.* **92**, 211107 (2008).
- [8] C. Argyropoulos, K. Q. Le, N. Mattiucci, G. D'Aguzzo, and A. Alu, *Phys. Rev. B* **87**, 205112 (2013).
- [9] G. Shvets, S. Trendafilov, J. B. Pendry, and A. Sarychev, *Phys. Rev. Lett.* **99**, 053903 (2007).
- [10] S. Kawata, Y. Inouye, and P. Verma, *Nat. Photonics* **3**, 388 (2009).
- [11] V. S. Volkov, S. I. Bozhevolnyi, S. G. Rodrigo, L. Martín-Moreno, F. J. Garcia-Vidal, E. Devaux, and T. W. Ebbesen, *Nano Lett.* **9**, 1278 (2009).
- [12] T. Søndergaard, S. I. Bozhevolnyi, J. Beermann, S. M. Novikov, E. Devaux, and T. W. Ebbesen, *Nano Lett.* **10**, 291 (2010).
- [13] E. Verhagen, L. K. Kuipers, and A. Polman, *Nano Lett.* **10**, 3665 (2010).
- [14] M. I. Stockman, *Phys. Rev. Lett.* **93**, 137404 (2004).
- [15] H. Choo, M. K. Kim, M. Staffaroni, T. J. Seok, J. Bokor, S. Cabrini, P. J. Schuck, M. C. Wu, and E. Yablonovitch, *Nat. Photonics* **6**, 838 (2012).
- [16] T. Søndergaard, S. M. Novikov, T. Holmgaard, R. L. Eriksen, J. Beermann, Z. Han, K. Pedersen, and S. I. Bozhevolnyi, *Nat. Commun.* **3**, 969 (2012).
- [17] T. Søndergaard and S. I. Bozhevolnyi, *New J. Phys.* **15**, 013034 (2013).
- [18] A. J. Babadjanyan, N. L. Margaryan, and K. V. Nerkararyan, *J. Appl. Phys.* **87**, 3785 (2000).
- [19] D. K. Gramotnev, *J. Appl. Phys.* **98**, 104302 (2005).
- [20] K. C. Vernon, D. K. Gramotnev, and D. F. Pile, *J. Appl. Phys.* **101**, 104312 (2007).
- [21] N. A. Issa and R. Guckenberger, *Plasmonics* **2**, 31 (2007).
- [22] D. K. Gramotnev, D. F. P. Pile, M. W. Vogel, and X. Zhang, *Phys. Rev. B* **75**, 035431 (2007).
- [23] D. Pile and D. K. Gramotnev, *Appl. Phys. Lett.* **89**, 041111 (2006).
- [24] D. K. Gramotnev, M. W. Vogel, and M. I. Stockman, *J. Appl. Phys.* **104**, 034311 (2008).
- [25] CONCERTO 7.0 (Vector Field Limited, Oxford, UK, 2008).
- [26] Here, $\varepsilon_{\text{eff}}(z), \mu_{\text{eff}}(z)$ stand for the parallel components of effective-medium parameters.
- [27] F. J. Garcia-Vidal, L. Martín-Moreno, and J. B. Pendry, *J. Opt. A Pure Appl. Opt.* **7**, S97 (2005).
- [28] J. T. Shen, P. B. Catrysse, and S. Fan, *Phys. Rev. Lett.* **94**, 197401 (2005).
- [29] S. Xiao, Q. He, X. Huang, and L. Zhou, *Metamaterials* **5**, 112 (2011).
- [30] Z. Song, Q. He, S. Xiao, and L. Zhou, *Appl. Phys. Lett.* **101**, 181110 (2012).
- [31] We cannot use the model to study the systems at very low frequencies where the PEC fails to describe a good metal.
- [32] See, e.g., D. J. Griffiths, *Introduction to Quantum Mechanics* (Prentice Hall, Upper Saddle River, NJ, 1995).
- [33] R. Malureanu, M. Zalkovskij, Z. Song, C. Gritti, A. Andryeuskii, Q. He, L. Zhou, P. U. Jepsen, and A. V. Lavrinenko, *Opt. Express* **20**, 22770 (2012).
- [34] H.-T. Chen, J. Zhou, J. F. O'Hara, F. Chen, A. K. Azad, and A. J. Taylor, *Phys. Rev. Lett.* **105**, 073901 (2010).
- [35] Z. Song and B. Zhang, *Opt. Express* **22**, 6519 (2014).

- [36] See Supplemental Material at <http://link.aps.org/supplemental/10.1103/PhysRevB.90.045110> for the additional oblique-incidence FDTD simulations.
- [37] B. Zhu, S. Tang, S. Xiao, and L. Zhou (unpublished).
- [38] M. A. Ordal, L. L. Long, R. J. Bell, S. E. Bell, R. R. Bell, R. W. Alexander, and C. A. Ward, *Appl. Opt.* **22**, 1099 (1983).
- [39] Y. Zhang, C. Li, and M. Loncar, *Opt. Lett.* **38**, 646 (2013).